Research Square

Preprints are preliminary reports that have not undergone peer review.
They should not be considered conclusive, used to inform clinical practice,
or referenced by the media as validated information.

Negative Enrichment of Ferroptosis Gene Sets and Identification of Core Spermatogenic Dysfunction Genes Under Hypothesis-Space Constraints: Multi-Cohort Consistency of ICA1 Downregulation and Virtual Knockout Evidence of PRM2/GPX4 Perturbation in Spermatids

Guozhong Zhang

guozhongz504@gmail.com

Panzhihua Maternal and Child Health Hospital

Yonghong Zi

Panzhihua Maternal and Child Health Hospital

Article

Keywords: non-obstructive azoospermia, spermatogenic impairment, ferroaging, ICA1, spermatids, GPX4, virtual knockout, interpretability

Posted Date: November 27th, 2026

DOI: https://doi.org/10.21203/rs.3.rs-11871498/v1

License: This work is licensed under a Creative Commons Attribution 4.0 International License.
Read Full License

Additional Declarations: No competing interests reported.

Abstract

Non-obstructive azoospermia (NOA) is the most severe form of male infertility. Its molecular basis is heterogeneous, and few implicated signals have produced clinically actionable targets. We tested whether a 95-gene ferroaging set is differentially expressed as a whole in spermatogenic dysfunction; a negative result then defines the hypothesis space for candidate screening. Discovery used testicular biopsies GSE145467 (10 normal vs. 10 severely impaired); validation used four independent cohorts (GSE9210, GSE45885, GSE160749, GSE6872), human single-cell data GSE112013 (6,490 cells, 3 donors), and mouse GSE109033 (4,651 cells, 3 replicates). Analyses combined limma ($|\log_2 FC|>0.585$, FDR < 0.05), hypergeometric and fry self-contained tests, LASSO/SVM-RFE/random-forest screening within a 41-gene restricted set (200 stratified bootstraps), multi-cohort directional validation, a ferroaging score, single-cell annotation with cross-species validation, and scTenifoldKnk virtual knockout. The 95-gene set was not globally enriched in GSE145467 (41 observed vs. ~40 expected; hypergeometric P = 0.30; fry P = 0.48) or GSE45885 (P = 0.59). The three learners intersected on ICA1 and PPP2R2B; genome-wide, neither was selected across 7 feature pools, and both had a LASSO bootstrap frequency of 0. ICA1 was directionally consistent with discovery in all four validation cohorts (8/8 comparisons; Stouffer P rank 2/95). The ferroaging score rose with spermatogenic-arrest grade (Spearman ρ = 0.557, P = 0.0017). ICA1 localized to spermatids in human (mean 1.27, detection 87.0%) and mouse (0.97, 85.5%). Virtual knockout of ICA1 upregulated PRM2 and GPX4 (FDR < 0.05). ICA1 is therefore the interpretable core candidate within the ferroaging space, and the PRM2/GPX4 perturbation is a testable mechanism.

Introduction

Non-obstructive azoospermia (NOA) is defined by the absence of spermatozoa in the ejaculate from impaired spermatogenesis and is the most severe form of male infertility[1–3]. Its molecular basis spans chromosomal and genetic abnormalities and idiopathic cases[1,4,5], and this heterogeneity appears in the transcriptional and post-transcriptional changes reported in affected testicular tissue, including dysregulated circular RNAs and RNA-binding proteins[6–8]. Clinically actionable targets remain scarce[1,9], which has motivated mapping the molecular landscape of impaired spermatogenesis by high-throughput methods[3,10].

Transcriptomic profiling comparing normal and impaired testicular tissue has produced candidate genes and pathway signatures[5–7]. Such differential signals are confounded by shifts in cell composition: the proportion of spermatogenic to somatic cells differs between normal and impaired tissue, and single-cell and single-nucleus studies show stage-specific germ-cell subtypes and distinct Sertoli-cell states whose abundances change in NOA[11–13]. Existing work has relied on single cohorts and single strategies with little cross-platform, cross-tissue, or cross-species validation of directional consistency, so candidates reproduce poorly. Ferroptosis-related gene sets have been used for candidate screening in spermatogenic impairment[14–16], but whether these programs are coordinately activated at the set level has not been tested.

Composite sets such as ferroaging are assembled by merging genes from several sources, so their boundaries are ambiguous and treating them as pathways carries an a priori labeling risk. Ferroaging describes an iron-driven aging trajectory in which age-related iron accumulation fuels chronic lipid peroxidation orchestrated by ACSL4, promoting senescence and functional decline[17]; related formulations tie iron dyshomeostasis, lipid peroxidation, and senescence phenotypes across tissues[18,19] and extend to age-related and inflammatory conditions[20–22]. The testis supports a connection between iron-dependent lipid peroxidation and spermatogenic failure: ferroptosis inhibition restores spermatogenesis in busulfan-treated mice[23], and elevated Sertoli-cell ferroptosis signaling is implicated in NOA[15]. Because ferroaging is defined as the union of ferroptosis, iron-homeostasis, and senescence genes, its boundary reflects list curation, not an established pathway.

Enrichment tests based on hypergeometric and self-contained statistics determine whether a set is differentially expressed as a whole, separating pathway evidence from candidate provenance. Sensitivity across multiple ferroptosis, iron-homeostasis, and senescence sets is required because single-set results depend on list definition. When a set is not enriched overall, the reasonable move is to treat it as a restricted hypothesis space and screen interpretable candidates within it. This study therefore: (1) tests whether the ferroaging set is differentially expressed as a whole in spermatogenic dysfunction; (2) selects candidates within the restricted space by LASSO, SVM-RFE, and random forest; (3) evaluates their robustness genome-wide and under bootstrapping; and (4) characterizes interpretable candidates through multi-cohort directional consistency, single-cell localization, cross-species conservation, and virtual knockout. The study does not build a diagnostic model; it yields a falsifiable, experimentally testable mechanism and a framework for prioritizing candidates.

Materials and methods

Data sources

The cohorts are summarized in the following table. GSE145467 (Agilent 4×44K, common reference; 20 cases: 10 normal, 10 severely impaired) was the discovery cohort. Four cohorts served for validation: GSE9210 (Agilent 1A V2; 58 cases: 47 NOA, 11 OA), GSE45885 (Affymetrix HuGene 1.0 ST; 31 cases: 4 control, 27 arrest/SCOS with grading), GSE160749 (Affymetrix HuGene 2.1 ST, ejaculated sperm; 24 cases: 6 fertile, 12 astheno-/teratozoospermia, 6 unclassified), and GSE6872 (Affymetrix U133 Plus 2.0, ejaculated sperm; 21 cases: 13 normal, 8 severe teratozoospermia). Single-cell data were human GSE112013 (10x scRNA-seq, testis; 6,490 cells, 3 donors) and mouse GSE109033 (10x scRNA-seq, testis; 4,651 cells, 3 replicates).

Dataset	Tissue	Platform	Samples	Use
GSE145467	Testicular biopsy	Agilent 4×44K (common reference)	20: 10 normal, 10 severely impaired	Discovery
GSE9210	Testis	Agilent 1A V2 (common reference)	58: 47 NOA, 11 OA	Validation
GSE45885	Testicular biopsy	Affymetrix HuGene 1.0 ST	31: 4 control, 27 arrest/SCOS	Validation (arrest grading)
GSE160749	Ejaculated sperm	Affymetrix HuGene 2.1 ST	24: 6 fertile, 12 astheno-/teratozoospermia, 6 unclassified	Validation
GSE6872	Ejaculated sperm	Affymetrix U133 Plus 2.0	21: 13 normal, 8 severe teratozoospermia	Validation
GSE112013	Testis	10x scRNA-seq	6,490 cells, 3 donors	Localization & virtual knockout
GSE109033	Testis (mouse)	10x scRNA-seq	4,651 cells, 3 replicates	Cross-species

Preprocessing and differential analysis

Probes were mapped to gene symbols; when multiple probes mapped to one gene, the highest-mean probe was retained. One-color arrays (GSE45885, GSE160749) were $\log_2$ signals and quantile-normalized; GSE6872 MAS5 signals were $\log_2$-transformed. Two-color arrays (GSE145467, GSE9210) were sample-versus-common-reference $\log_2$ ratios; with a constant reference, group differences equal log-intensity differences. Differential analysis used limma with $|\log_2 FC|>0.585$ and Benjamini-Hochberg FDR < 0.05.

Ferroaging gene set and candidate set

The 95 ferroaging-related genes (FARGs) of Liu et al.[17] were used. Hypergeometric and limma fry self-contained tests assessed whole-set differential expression. The intersection of differentially expressed genes and FARGs defined the 41-gene candidate set.

Candidate screening and genome-wide robustness testing

Hypothesis-restricted screening. LASSO (glmnet, stratified 3-fold λ selection), SVM-RFE (linear kernel, elimination to 5 features), and random forest (1,000 trees, top 5 by MeanDecreaseAccuracy) were run on the 41 candidates; their intersection defined the candidate genes.

Genome-wide robustness testing. The three algorithms were repeated on all differentially expressed genes (4,777 at 2-fold; 7,900 at 1.5-fold) and top-15/20/30/50/100/200 FDR-ranked pools, recording candidate selection. LASSO with 200 stratified bootstraps was run on the 4,777 genes; selection frequencies were counted, and high-frequency genes were checked against ferroaging, ferroptosis, and aging sets.

Discriminative performance. Nested leave-one-out cross-validation was reported descriptively. The two groups were nearly completely separated (AUC = 1.000, degenerate confidence interval), so AUC was not used as evidence.

Multi-cohort validation and ferroaging score

Between-group $\log_2$ differences of candidate genes were computed in the four validation cohorts; directional consistency was the primary validation metric, transfer AUC secondary. The ferroaging score was the mean within-sample z-score of the 95 genes. Wilcoxon tests compared scores between groups; a Spearman trend test used spermatogenic-arrest grade in GSE45885.

Single-cell and cross-species analysis

The merged UMI table of GSE112013 (6,490 cells × 27,477 genes) was CPM-normalized and log1p-transformed. Marker genes of eight cell types were z-standardized and averaged; each cell was assigned to the highest-scoring type (> 0.25). Candidate genes were reported as mean expression and detection rate. Mouse GSE109033 (4,651 cells) was annotated with orthologous markers; Ica1/Ppp2r2b distributions were examined.

Virtual knockout

Spermatogonia, spermatocytes, and spermatids from GSE112013 (3,970 cells) were retained. Genes with detection ≥ 2% were kept, and candidate genes were retained. scTenifoldKnk built 10 regulatory networks (500 cells each); perturbation was quantified by CP decomposition (rank 3) and manifold alignment, with FDR < 0.05 significant.

Statistics and software

Analyses used R 4.6.1 (limma, glmnet, e1071, randomForest, pROC, clusterProfiler, org.Hs.eg.db, Matrix, scTenifoldKnk). Two-sided P < 0.05 was significant unless stated otherwise.

Results

The ferroaging gene set is not globally enriched in spermatogenic impairment

GSE145467 contributed 19,749 genes, yielding 7,900 differentially expressed genes at 1.5-fold and FDR < 0.05 (4,777 at 2-fold). Intersection with the 95 ferroaging genes (92 detectable) yielded 41 candidates. This intersection was not globally enriched: ~40 expected versus 41 observed (hypergeometric P = 0.30), and the fry self-contained test did not support global differential expression (P = 0.48). The same test was negative in GSE45885 (P = 0.59).

The ferroaging set is therefore not globally activated in spermatogenic impairment; it serves only as a source of candidate genes, not as a mechanistic claim. Within the 41 candidates, the most significant were PPP2R2B (log_2FC = − 2.51, FDR = 1.1×10^{-8}), ICA1 (− 3.10, 1.9×10^{-8}), FBXO31 (− 4.60, 4.9×10^{-8}), IRF9 (+ 1.48, 6.3×10^{-8}), and ATG3 (− 1.40, 7.6×10^{-8}) (Table 1, Figs. 1 and 2). GO enrichment concentrated on endothelial-cell migration, inflammatory-response regulation, chemotaxis, and positive regulation of apoptosis (Table 2).

Table 1
Ferroaging candidate genes (GSE145467; top 10 of 41, full list in Supplementary Table S2).

Gene	log2FC	FDR	Direction
PPP2R2B	−2.51	1.1×10^{-8}	Down
ICA1	−3.10	1.9×10^{-8}	Down
FBXO31	−4.60	4.9×10^{-8}	Down
IRF9	+ 1.48	6.3×10^{-8}	Up
ATG3	−1.40	7.6×10^{-8}	Down
DYRK1A	−1.46	4.8×10^{-7}	Down
MAPK1	−1.86	6.4×10^{-7}	Down
TNFAIP1	+ 1.33	6.7×10^{-7}	Up
BAP1	−1.74	1.3×10^{-6}	Down
SPATA2	−0.79	4.6×10^{-6}	Down

Table 2
GO biological process enrichment of the 41 candidate genes (top 5 terms).

Term	Gene ratio	FDR
Endothelial cell migration (GO:0043542)	8/41	2.9×10^{-4}
Regulation of inflammatory response (GO:0050727)	8/41	1.5×10^{-3}
Regulation of chemotaxis (GO:0050920)	6/41	1.5×10^{-3}
Myeloid leukocyte migration (GO:0097529)	6/41	1.5×10^{-3}
Positive regulation of apoptosis (GO:0043065)	8/41	1.6×10^{-3}

Candidates within the hypothesis space: ICA1 primary, PPP2R2B secondary

Among the 41 candidates, LASSO selected PPP2R2B, ATG3, ICA1, BCL6, and DYRK1A; SVM-RFE selected PPP2R2B, ICA1, IRF9, DYRK1A, and SPATA2; random forest selected ICA1, PPP2R2B, IRF9, FBXO31, and ATG3. The intersection was ICA1 and PPP2R2B (Table 3, Fig. 3), and it holds only within the ferroaging prior space.

Table 3
Selection by three algorithms within the hypothesis-restricted candidate set (41 genes).

Method	Selected genes
LASSO	PPP2R2B, ATG3, ICA1, BCL6, DYRK1A
SVM-RFE	PPP2R2B, ICA1, IRF9, DYRK1A, SPATA2
Random forest	ICA1, PPP2R2B, IRF9, FBXO31, ATG3
Intersection	ICA1 (primary), PPP2R2B (secondary)

ICA1 is the primary candidate because: (1) its effect size is directionally consistent and largest across all five cohorts; (2) its detection rate is highest in spermatids (87.0%), as is its mouse ortholog (85.5%); and (3) its virtual knockout produced an effective perturbation targeting PRM2 and GPX4. PPP2R2B showed a weaker effect in some cohorts and a negative virtual knockout, so it is secondary.

Genome-wide machine learning returns negative results

To test genome-wide discriminative power, the three algorithms were repeated on all differentially expressed genes and top-N pools. Neither ICA1 nor PPP2R2B was selected by LASSO, SVM-RFE, or random forest across 7 feature pools (4,777 and 7,900 genes, and top-15/20/30/50/100/200) (Table 4, Figure S2). In the 200-iteration LASSO bootstrap on 4,777 genes, both had a selection frequency of 0; the highest frequency was 43.5% (C10orf90), none reached 50%, and 2 reached 30%. None of the top 15 genes by frequency belonged to ferroaging, ferroptosis, or aging sets.

Table 4
Genome-wide robustness testing (whether candidate genes were selected).

Feature pool	Genes	LASSO	SVM-RFE	Random forest
2-fold DEG	4,777	Not selected	Not selected	Not selected
1.5-fold DEG	7,900	Not selected	Not selected	Not selected
top-15 (FDR)	15	Not selected	Not selected	Not selected
top-20 (FDR)	20	Not selected	Not selected	Not selected
top-30 (FDR)	30	Not selected	Not selected	Not selected
top-50 (FDR)	50	Not selected	Not selected	Not selected
top-100 (FDR)	100	Not selected	Not selected	Not selected
top-200 (FDR)	200	Not selected	Not selected	Not selected

In comparisons dominated by tissue-composition differences (differentially expressed genes ≈ 40%), genome-wide learning preferentially selects discriminative cell-type markers (C10orf90, SPATA18, LOXHD1) whose power reflects spermatogenic-versus-somatic cell proportions, not disease mechanism. Discriminative power and interpretability are therefore decoupled in this design. We select candidates within the hypothesis space that are interpretable, localizable, and testable by network perturbation.

ICA1 downregulation is directionally consistent across five cohorts

ICA1 was directionally consistent with discovery in all four validation cohorts (8/8 comparisons): GSE9210 (NOA vs. OA) − 1.33, GSE45885 (NOA vs. control) − 0.99, GSE160749 (oligozoospermia) − 0.19, and GSE6872 (teratozoospermia) − 2.60 (Table 5, Fig. 5). PPP2R2B was also consistent (− 0.13, − 0.41, − 0.13, − 2.35) with smaller magnitudes. Transfer AUC was 0.68–0.95, obtained with two genes and two highly divergent groups.

Table 5
Direction of candidate genes across five cohorts.

Cohort	n	ICA1 logFC	PPP2R2B logFC	Transfer AUC
GSE145467 (discovery)	20	−3.10	−2.51	—
GSE9210	58	−1.33	−0.13	0.93
GSE45885	31	−0.99	−0.41	0.79
GSE160749	24	−0.19	−0.13	0.68
GSE6872	21	−2.60	−2.35	0.95

Gene-level replication was limited. Comparing the direction of each of the 95 FARGs between discovery and the four validation cohorts, and combining signed P values by Stouffer's method, only 12 of 92 genes (13%) were concordant in all four cohorts (BAP1, CDO1, COX7A1, DUOX1, EPHA4, FBXO31, HMGB1, ICA1, KEAP1, PPP2R2B, S100A8, SNCA); 24 were concordant in 3/4, 37 in 2/4, 17 in 1/4, and 2 in 0/4. ICA1's combined P ranked 2nd among 95 (behind FBXO31), and PPP2R2B ranked 6th (Table 6).

Table 6
Gene-set sensitivity analysis (discovery cohort GSE145467; 19,749 genes, 7,900 DEG).

Gene set	Genes in set	DEG	Expected	Hypergeometric P	Concordant 4/4	Contains ICA1
FARG95	92	41	36.8	0.21	12	Yes
FARG95 (minus aging)	88	40	35.2	0.17	11	Yes
FARG95 ∪ KEGG ferroptosis ∪ aging	143	61	57.2	0.29	12	Yes
FARG95 ∩ KEGG ferroptosis	5	1	2.0	0.92	0	No
KEGG ferroptosis	40	18	16.0	0.31	0	No
Iron homeostasis	32	17	12.8	0.09	0	No
Aging	21	4	8.4	0.99	1	No

Gene-set sensitivity. Seven iron/ferroptosis/aging sets showed no global enrichment in the discovery cohort (hypergeometric P = 0.09–0.99): FARG95 P = 0.21 (41/92, expected 36.8), FARG95 minus aging P = 0.17, FARG95 ∪ KEGG-ferroptosis ∪ aging P = 0.29, KEGG ferroptosis P = 0.31, iron homeostasis P = 0.09, aging P = 0.99 (Table 6). ICA1 appears only in FARG95, not in KEGG ferroptosis, iron homeostasis, or aging; the FARG95–KEGG-ferroptosis intersection is 5 genes. ICA1's ferroaging attribution therefore depends on the list and sits at the prior-label level.

The ferroaging score rises with spermatogenic-arrest grade

In GSE45885, the 95-gene ferroaging score rose with arrest grade (control − 0.08, post-meiotic arrest − 0.17, meiotic arrest − 0.11, Sertoli-cell-only syndrome + 0.33; Spearman ρ = 0.557, P = 0.0017). In GSE9210, the score was higher in NOA than OA ($P = 4.4\times10^{-9}$); the three smaller cohorts did not reach significance. This score reflects the overall level of the 95 genes and is independent of individual candidate conclusions.

ICA1 localizes to spermatids and is conserved in mice

GSE112013 comprised 6,490 cells from 3 donors, annotated as 2,431 spermatids, 918 spermatocytes, 621 spermatogonia, 574 peritubular myoid cells, 455 interstitial cells, 390 endothelial cells, 353 macrophages, 248 Sertoli cells, and 500 unannotated cells (Fig. 6). ICA1 was highest in spermatids (mean 1.27, detection 87.0%), then Sertoli cells (0.80, 58.9%) and endothelial cells (0.41, 39.0%); the Sertoli signal may reflect ambient RNA of spermatogenic origin. PPP2R2B was also highest in spermatids (1.00, 75.4%). In mouse GSE109033, Ica1 was highest in spermatids (0.97, 85.5%) and Ppp2r2b at 84.6%, matching the human pattern (Figure S1).

Virtual knockout of ICA1 perturbs PRM2 and GPX4

Virtual knockout of ICA1 in 3,970 spermatogenic cells from GSE112013 produced three significantly perturbed genes (FDR < 0.05): ICA1 downregulated, PRM2 and GPX4 upregulated (Fig. 7). PRM2 encodes protamine 2, the core protein of sperm chromatin condensation; GPX4 is the key ferroptosis antioxidant enzyme. ICA1 therefore couples vesicular transport, chromatin condensation, and redox homeostasis. Virtual knockout of PPP2R2B produced no perturbation: it has no outgoing edges in the wild-type network, knockout does not alter network structure, and all P values were set to 1.

Discussion

The 95-gene ferroaging set showed no global differential enrichment under the hypergeometric or fry tests, replicated across two cohorts. Ferroaging activation is therefore not a mechanism for impaired spermatogenesis. The negative result held across seven sensitivity sets, and ICA1 appeared only in FARG95, not in canonical KEGG ferroptosis, iron-homeostasis, or aging collections. Its ferroaging assignment is a list-level prior label, not pathway evidence, consistent with curated aging and ferroptosis annotations only partially overlapping the programs operative in a tissue. The ferroaging set is a prior tool for narrowing the hypothesis space.

The ferroaging score that rises with impairment severity ($\rho = 0.557$) reflects changes in the proportional composition of spermatogenic cells, because cell-composition shifts dominate transcriptional signal in testicular disease[26]. This is separate from candidate-gene conclusions.

Genome-wide, ICA1 and PPP2R2B were not selected by any algorithm, their bootstrap frequencies were zero, and no frequently selected gene belonged to iron-aging, ferroptosis, or senescence sets. Genome-wide learning thus captures cell-type composition markers, not disease-mechanism genes. Classifiers trained on whole-genome data reach high accuracy without causal interpretation, whereas approaches that incorporate biochemical constraints recover known mechanisms with predictive performance[27]. In the normal-versus-severely-impaired comparison, differentially expressed genes were ≈ 40% of the data, and the discriminative signal was driven by spermatogenic-versus-somatic proportions, documented repeatedly in single-cell studies of spermatogenic failure. High AUC and biological interpretability are therefore misaligned in this design, and AUC is not used as evidence.

The nested leave-one-out AUC of 1.000 and its degenerate confidence interval reflect a near-complete-separation design. The transfer AUC (0.68–0.95) mirrors the instability of expression-based classifiers across cohorts and platforms[24]. The candidate-screening paradigm — an a priori-restricted space with localizability and network perturbability — offers an alternative to purely discriminative strategies for transcriptomic comparisons dominated by compositional differences.

ICA1 is the core candidate: it changed directionally consistently in all eight comparisons across five cohorts and ranked 2nd of 95 by Stouffer combined P, versus PPP2R2B at 6th with a smaller effect and a negative virtual knockout. Single-cell and cross-species analyses placed ICA1 highest in spermatids in human and mouse (detection 87.0% and 85.5%), supporting conserved localization and matching the transcriptional changes consistently observed in spermatids across models of impaired spermatogenesis[26]. Sertoli-cell signals may reflect ambient RNA, and Sertoli cells are sensitive to age- and stress-related transcriptional perturbation[28].

Virtual knockout upregulated PRM2 and GPX4, indicating ICA1 couples vesicle transport, chromatin condensation, and redox homeostasis; this is the most biologically interesting finding and the one requiring experimental validation, and its computational, predictive nature is explicit. The hypothesis is plausible given ICA1's roles in exocytosis and vesicular transport and their relation to acrosome formation and protamine replacement. Its connection to ferroptosis is indirect, illustrated by the routes through which mitochondrial dysfunction and lipid peroxidation converge on ferroptosis in germ cells[29].

Replication at the gene level was limited: 12 of 92 genes were directionally consistent across all four validation cohorts. ICA1 and FBXO31 are representative reproducible candidates. Existing evidence supports a reproductive function for ICA1, including acrosomal and nuclear defects and reduced fertility in Ica1l-deficient males[30].

Validation cohorts were small and differed in platform and reference design (two-color common-reference labeling, single-color quantile normalization, MAS5 transformation); cross-cohort directional consistency remains susceptible to batch effects and composition differences[24]. The virtual-knockout result rests on scTenifoldKnk's network assumptions and a rank-3 CP decomposition, so the PRM2/GPX4 perturbations require experimental confirmation by qPCR, Western blot, and ICA1 knockdown or overexpression in spermatogenic cells or animal models[29,30]. The absence of protein, methylation, and functional data means the regulatory level of ICA1 downregulation (transcriptional, post-transcriptional, or compositional) is undetermined, a key direction given the prominence of post-transcriptional and epigenetic layers in spermatogenic dysfunction[31]. The clinical value of the ferroaging score and candidates requires evaluation in prospective cohorts with complete histological grading[32,33].

Declarations

Author contributions

G.Z. conceived and designed the study, performed the bioinformatics analyses, and wrote the manuscript. Z.Y. contributed to data curation, validation, and visualization. All authors reviewed and approved the final manuscript.

Competing interests

The authors declare no competing interests.

Ethics declarations

Ethics approval and consent to participate. All data were obtained from publicly available, de-identified datasets deposited in the NCBI Gene Expression Omnibus (GEO). The original studies from which these datasets derive obtained ethical approval and informed consent from their respective institutional review boards; details are available in the corresponding original publications. This study involved no new human subjects, animal experiments, or tissue collection; therefore no additional ethical approval or informed consent was required.

Consent for publication. Not applicable.

Data availability. All data are publicly available from GEO (accession numbers GSE145467, GSE9210, GSE45885, GSE160749, GSE6872, GSE112013, and GSE109033). Analysis scripts are available from the corresponding author upon reasonable request.

Code availability. Analysis scripts are available from the corresponding author upon reasonable request.

Funding. This work was supported by the Health Commission of Sichuan Province Medical Science and Technology Program (grant no. 25QNMP021).

References

1. Chiba, K., Enatsu, N. & Fujisawa, M. Management of non-obstructive azoospermia. *Reproductive Med. Biology*. **15**, 165–173 (2016).
2. Klami, R., Mankonen, H. & Perheentupa, A. Successful microdissection testicular sperm extraction for men with non-obstructive azoospermia. *Reprod. Biol.* **18**, 137–142 (2018).
3. Han, B. et al. Infertility network and hub genes for nonobstructive azoospermia utilizing integrative analysis. *Aging* **13**, 7052–7066 (2021).
4. Peña, V. N., Kohn, T. P. & Herati, A. S. Genetic mutations contributing to non-obstructive azoospermia. *Best Pract. Res. Clin. Endocrinol. Metab.* **34**, 101479 (2020).
5. D'Aurora, M. et al. Testis transcriptome modulation in Klinefelter patients with hypospermatogenesis. *Sci. Rep.* **7**, 45729 (2017).

6. Bo, H. et al. Testicular biopsies microarray analysis reveals circRNAs are involved in the pathogenesis of non-obstructive azoospermia. *Aging* **12**, 2610–2625 (2020).
7. Peng, F. et al. An artificial neural network model to diagnose non-obstructive azoospermia based on RNA-binding protein-related genes. *Aging* **15**, 3120–3140 (2023).
8. Xu, N. et al. An integrated transcriptomic analysis unveils the regulatory roles of RNA binding proteins during human spermatogenesis. *Front. Endocrinol.* **16**, 1522394 (2025).
9. Li, J. Y. et al. Basonuclin 1 deficiency causes testicular premature aging: BNC1 cooperates with TAF7L to regulate spermatogenesis. *J. Mol. Cell Biol.* **12**, 71–83 (2020).
10. Nelson, B., Smith, H., Smith, R. P. & Kohn, T. P. Emerging diagnostics tools for severe male infertility and non-obstructive azoospermia. *Urology* **213**, 53–57 (2026).
11. Wang, S. et al. scRNA-seq and scATAC-seq reveal that Sertoli cell mediates spermatogenesis disorders through stage-specific communications in non-obstructive azoospermia. *eLife* 13 (2025).
12. Wu, X. et al. scRNA-seq-based transcriptome profiling and relevant bioinformatics approaches to uncover novel insights in studying human spermatogenesis. *Adv. Exp. Med. Biol.* **1469**, 173–205 (2025).
13. Yu, J. et al. Integrated single-cell and bulk transcriptomic analyses reveal UTF1-associated spermatogenic dysfunction and identify ACTRT2 and AKAP4 as biomarkers in non-obstructive azoospermia. *Front. Genet.* **17**, 1975399 (2026).
14. Shen, H. P. et al. Exploring the mechanisms of ferroptosis in non-obstructive azoospermia based on bioinformatics and machine learning. *Zhonghua Nan Ke Xue*. **29**, 874–880 (2023).
15. Bo, H. et al. Single-cell, spatial and bulk transcriptome data analysis revealed LINC00467-mediated Sertoli cell ferroptosis is a potential therapeutic target and biomarker for azoospermia. *Free Radic. Biol. Med.* **240**, 650–662 (2025).
16. Zhu, X., Wang, S., Li, T., Li, Y. & Zhou, T. BDE-47 and male infertility: integrated network toxicology, single-cell transcriptomics, and in vitro evidence of GSTM1 downregulation and ferroptosis-related molecular remodeling in Leydig cells. *Front. Immunol.* **17**, 1956997 (2026).
17. Liu, L. et al. Vitamin C inhibits ACSL4 to alleviate ferro-aging in primates. *Cell Metabol.* **38**, 673–693e17 (2026).
18. Gao, S. et al. Ferro-aging: a novel paradigm linking iron overload, lipid peroxidation and cellular senescence. *Free Radic. Biol. Med.* **253**, 817–829 (2026).
19. Liu, L., Qu, J., Liu, G. H. & Zhang, W. Ferro-aging: iron-lipid axis in systemic decline. *Trends Endocrinol. Metabolism*. https://doi.org/10.1016/j.tem.2026.09.009 (2026).
20. Liang, S. et al. Ferro-aging: a potential driver of degenerative bone and joint diseases. *Cell. Communication Signal.* **24** (2026).
21. Tian, D. et al. *A putative iron-related evolving framework in Alzheimer's disease: from iron dyshomeostasis and ferro-aging to ferroptosis* (Journal of Alzheimer's Disease, 2026).

22. Wang, Q., Wang, N., Yan, H. & Yuan, J. Identification of ferro-aging-related biomarkers for ulcerative colitis through integrated machine learning, single-cell analysis, and spatial transcriptomics. *FASEB J.* **40**, e72255 (2026).
23. Feng, Y. Q. et al. NAD+ precursors promote the restoration of spermatogenesis in busulfan-treated mice through inhibiting Sirt2-regulated ferroptosis. *Theranostics* **14**, 2622–2636 (2024).
24. Quach, A. et al. No reliable gene expression biomarkers of current or impending neurocognitive impairment in peripheral blood monocytes of persons living with HIV. *J. Neurovirol.* **24**, 350–361 (2018).
25. Cheung, N. Polycomb-derived posttraumatic stress disorder (PTSD) signals diverge from classical aging pathways and converge on neuroimmune genes. *Cureus* **18**, e112717 (2026).
26. Xu, X. et al. Dissection of obesity-induced spermatogenic dysfunction at single-cell resolution. (2026). https://doi.org/10.1111/andr.70378
27. Kavvas, E. S., Yang, L., Monk, J. M., Heckmann, D. & Palsson, B. O. A biochemically-interpretable machine learning classifier for microbial GWAS. *Nat. Commun.* **11**, 2580 (2020).
28. Huang, D. et al. A single-nucleus transcriptomic atlas of primate testicular aging reveals exhaustion of the spermatogonial stem cell reservoir and loss of Sertoli cell homeostasis. *Protein Cell.* **14**, 888–907 (2023).
29. Li, T. et al. FBXO39 knockdown promotes spermatogenesis impairment by inducing mitochondrial dysfunction and ferroptosis via inhibiting KDM5A ubiquitination and regulating H3K4me3 demethylation. *Cell Biol. Toxicol.* **42** (2026).
30. He, J., Xia, M., Tsang, W. H., Chow, K. L. & Xia, J. ICA1L forms BAR-domain complexes with PICK1 and is crucial for acrosome formation in spermiogenesis. *J. Cell Sci.* **128**, 3822–3836 (2015).
31. Bilmez, Y., Talibova, G., Tire, B. & Ozturk, S. Histone lysine methyltransferases and their specific methylation marks show significant changes in mouse testes from young to older ages. *Biogerontology* **26**, 42 (2025).
32. Dong, F., Ping, P., Wang, S. Q., Ma, Y. & Chen, X. F. RPS14 as an aging-related biomarker for early-onset alterations of testicular senescence-associated genes in spermatogenic dysfunction at childbearing age. *Journals Gerontol. Ser. A* **81** (2026).
33. Alfano, M. et al. Testis molecular pathways in CAIS unveil testosterone/estradiol on germ cell tumor risk in non-obstructive azoospermia. *J. Clin. Endocrinol. Metab.* **111**, 388–404 (2026).

Figures

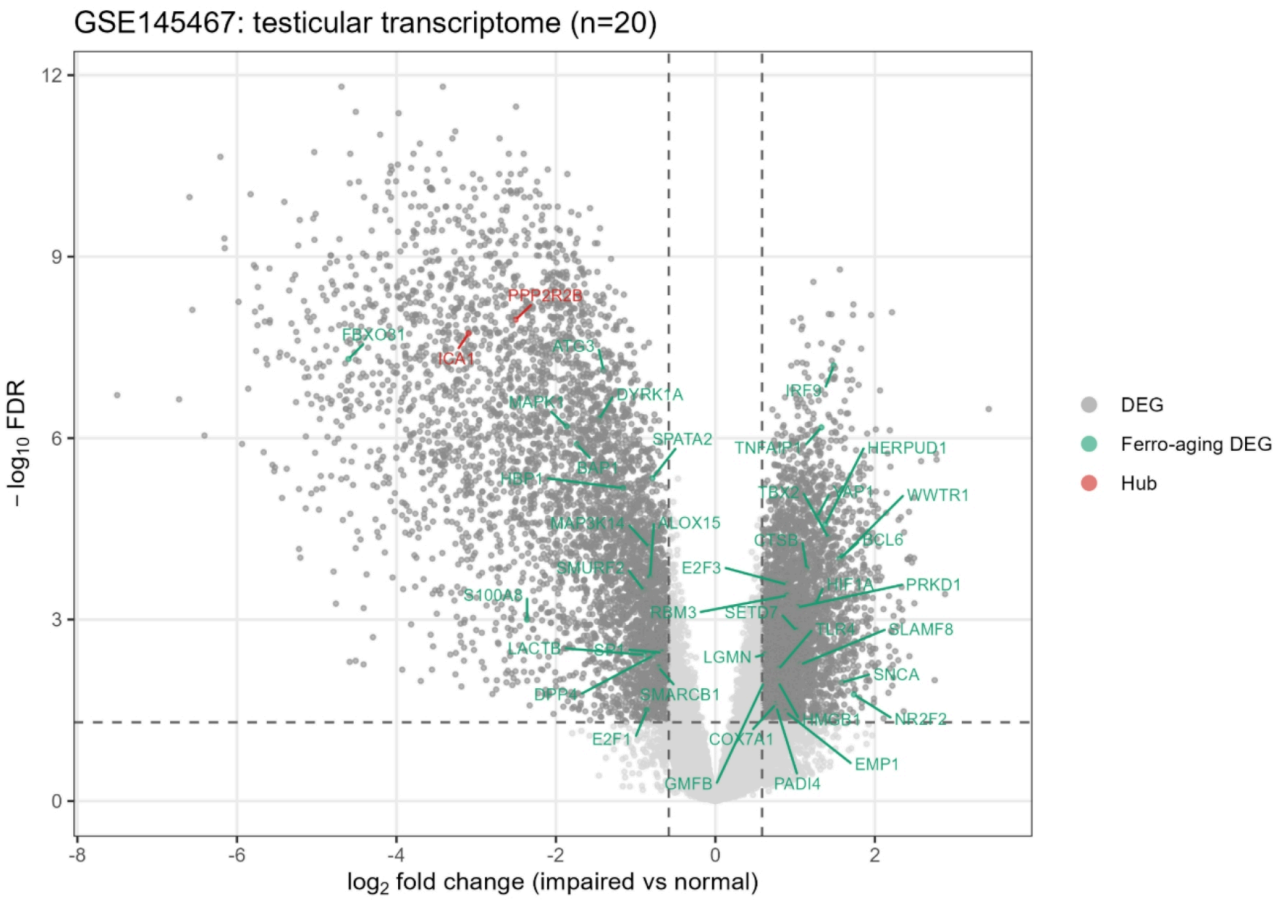

Figure 1

Differential expression in the discovery cohort (GSE145467, 20 testicular biopsies: 10 normal vs. 10 severely impaired spermatogenesis). Volcano plot of log2 fold change (impaired vs. normal; x-axis) against −log10 false discovery rate (FDR; y-axis) from limma. Gray dots, all tested genes; green dots, differentially expressed ferro-aging genes; red dots and labels, hub genes PPP2R2B and ICA1. Horizontal dashed line, FDR = 0.05; vertical dashed lines, |log2FC| = 0.585 (1.5-fold).

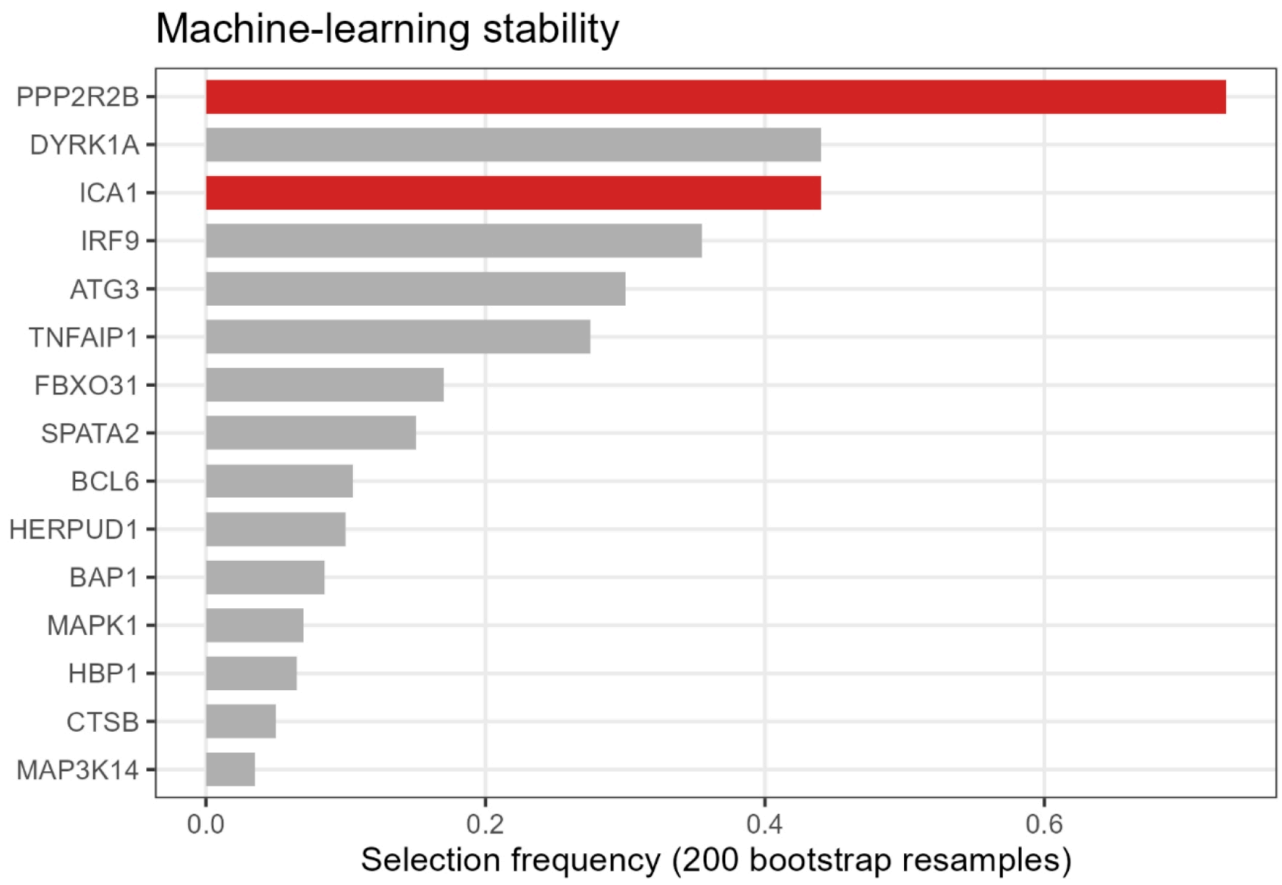

Figure 3

Machine-learning stability within the hypothesis-restricted candidate set. Selection frequency of each candidate gene across 200 bootstrap resamples of the 41-gene set, combining LASSO, SVM-RFE, and random forest. PPP2R2B and ICA1 are the most frequently selected; their intersection defines the hub genes.

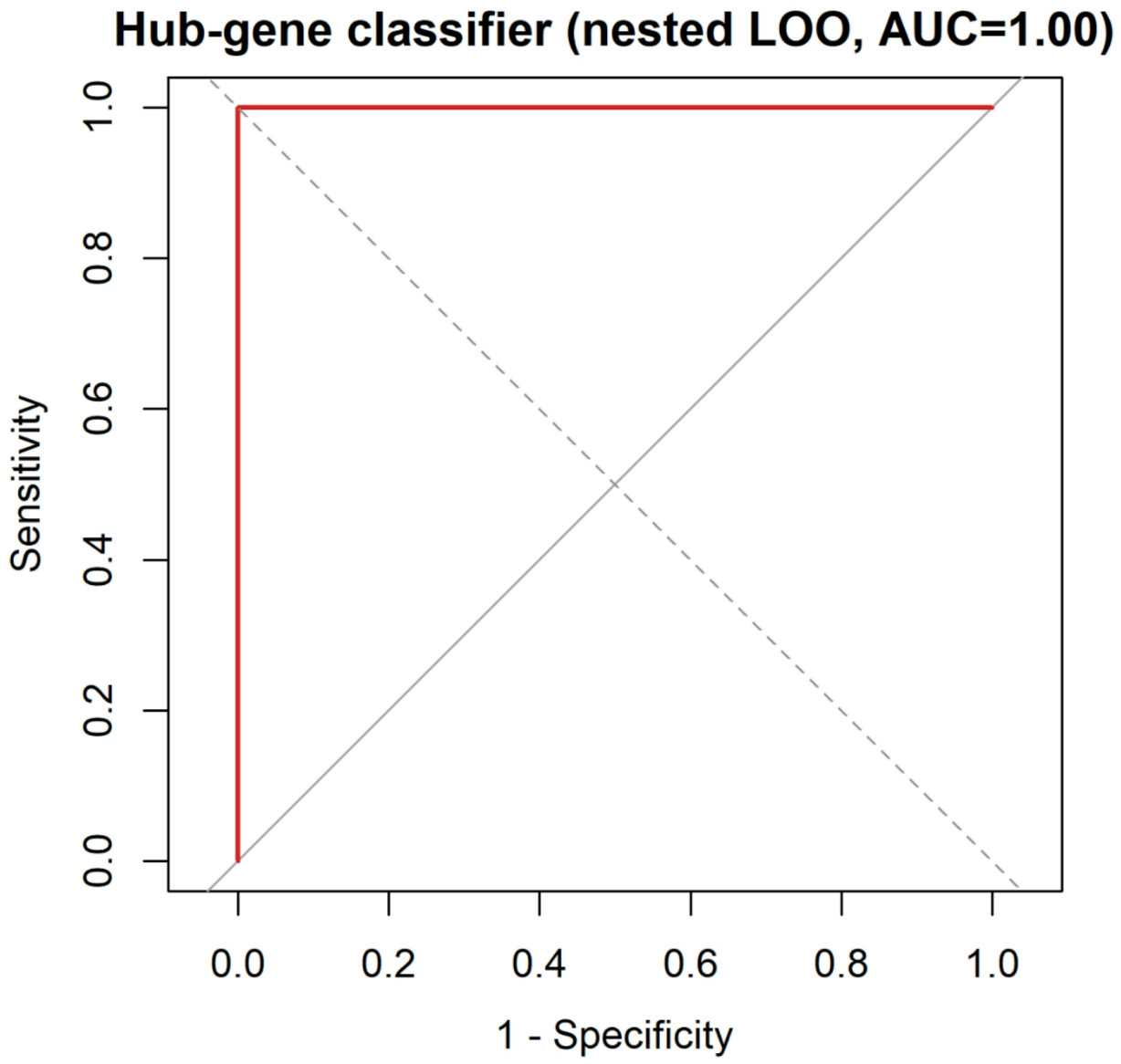

Figure 4

Receiver operating characteristic (ROC) curve of the hub-gene classifier (ICA1 and PPP2R2B) under nested leave-one-out cross-validation in the discovery cohort (GSE145467). AUC = 1.000 with the two groups nearly completely separated. Diagonal dashed line, chance level (AUC = 0.5).

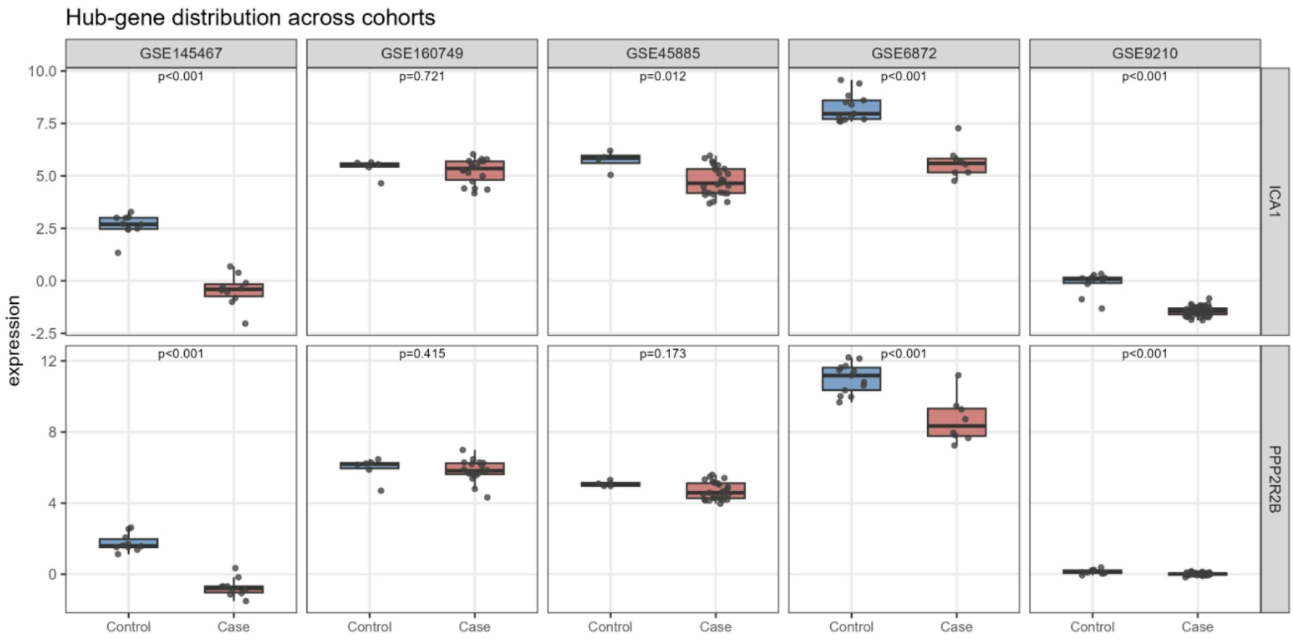

Figure 5

Expression of ICA1 (top row) and PPP2R2B (bottom row) across the five cohorts, as box plots with individual samples. Panels: GSE145467, GSE160749, GSE45885, GSE6872, GSE9210. Boxes span the interquartile range with the median line; whiskers extend to 1.5× IQR. Two-sided Wilcoxon rank-sum tests; P values above each panel.

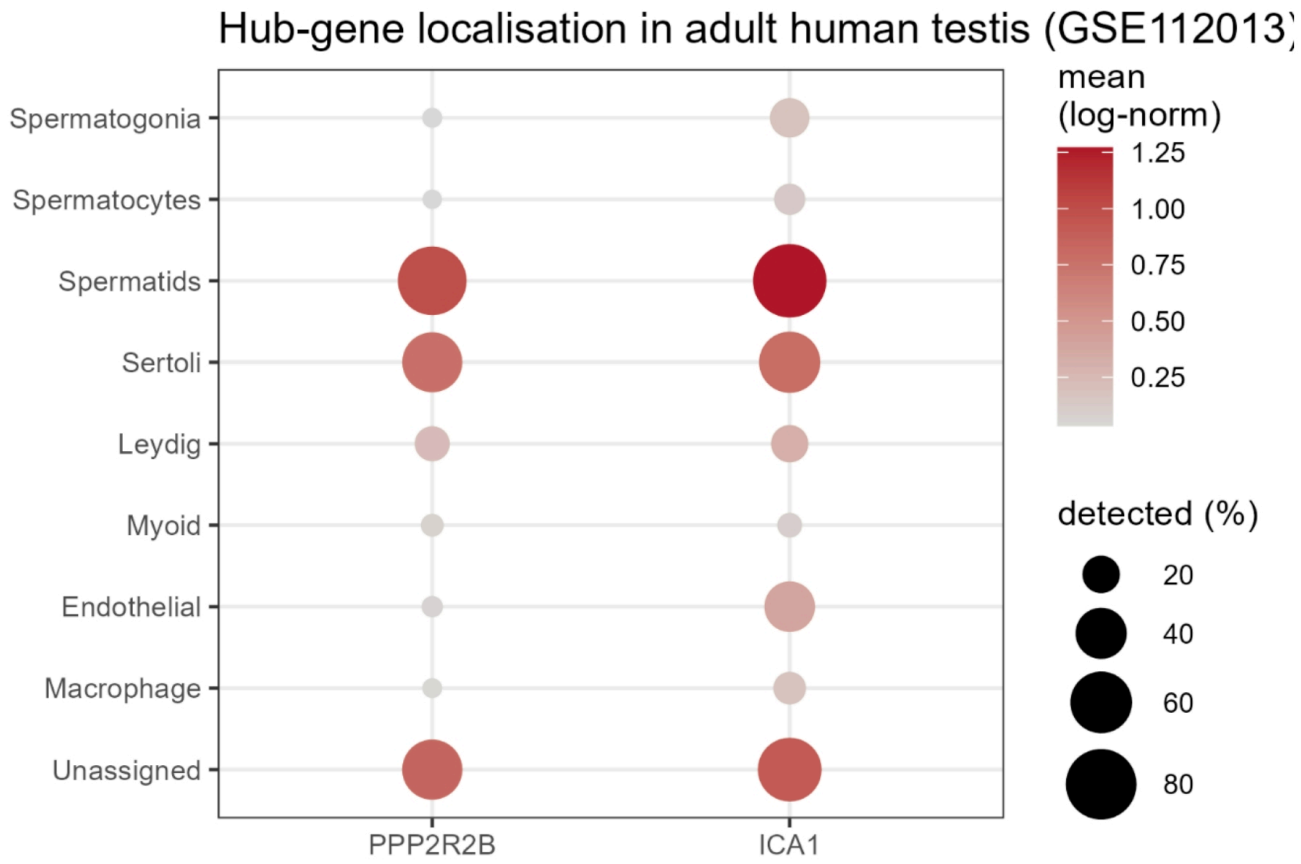

Figure 6

Localization of ICA1 and PPP2R2B across adult human testicular cell types (GSE112013; 6,490 cells from 3 donors). Dot plot of mean expression (color) and percentage of expressing cells (size) in nine cell types. Both genes are highest in spermatids.

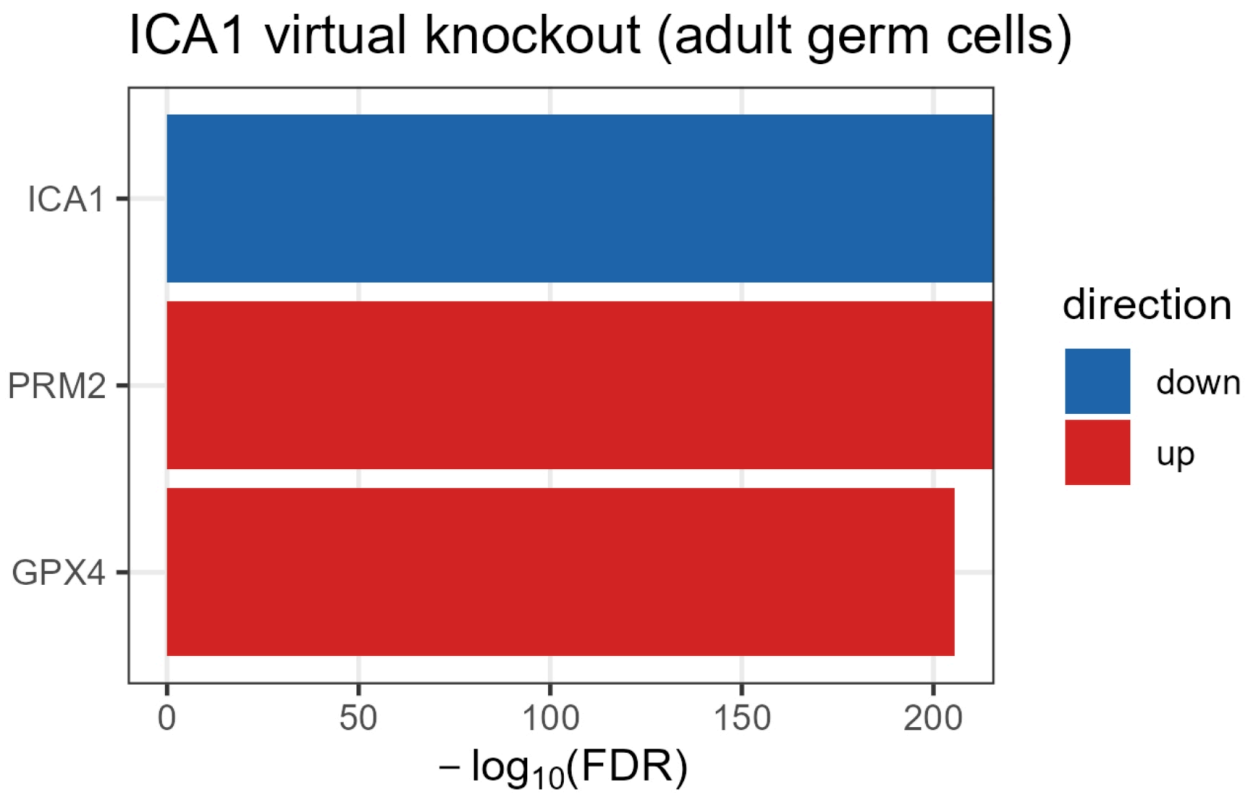

Figure 7

Virtual knockout of ICA1 in adult germ cells (GSE112013; 3,970 spermatogonia, spermatocytes, spermatids). Genes perturbed at FDR < 0.05 by scTenifoldKnk (CP decomposition, rank 3). Bar length, −log10 FDR; blue, downregulated (ICA1); red, upregulated (PRM2, GPX4).

Supplementary Files

This is a list of supplementary files associated with this preprint. Click to download.

- floatimage8.jpeg
- floatimage9.png